Collection SFN **7** (2007) s221–s240

Neutron grazing incidence techniques for nano-science

V. Lauter-Pasyuk[1,2]

[1] *Physik Department, TU München, 85747 Garching, Germany*
[2] *Institut Laue-Langevin, 6 rue Jules Horowitz, 38042 Grenoble, France*

1 INTRODUCTION

Grazing-angle neutron scattering and properties of structures with reduced in one direction dimensionality are constantly developing fields of modern condensed-matter research. The developments of the advanced methods of thin films Õ preparation created an avalanche of demand for the characterization of thin films properties. Amongst the large body of complementary and competing techniques the neutron scattering techniques have a number of advantages. They can be summarized as follows:

- contrast variation between different elements or isotopes due to different cross sections of different atoms and the interaction with nuclei rather than with diffuse electron cloud seen by e.g. X-rays,
- very high penetration and access to buried interfaces due to a very low absorption cross section,
- direct access to the layer magnetization distribution via the magnetic dipole interaction of the neutron spin with atomic magnetic moments,
- non-destructive even for delicate biological materials.

Since early 80-s neutron specular reflectometry has been developed into a commonly used experimental technique for the investigation of thin films and multilayers. Now a days reflectometers are used for the investigation of magnetic systems, organic materials, polymers and biological films (see for review [1]). At present only conventional reflectometry is routinely used to investigate the structure of films or multilayers *perpendicular* to their surfaces with fields of application ranging from magnetic multilayers to biological films. Specular reflection delivers information about the depth profile of the mean scattering length density (SLD) averaged over the whole sample surface. However, in reality *pure* specular reflection does not exist, because real surfaces or interfaces are not ideal and cannot be atomically flat. Therefore, specular reflection is *always* accompanied by off-specular scattering.

The full range of off-specular scattered intensity became accessible mainly due to the use of multidetectors. Off-specular scattering probes the *lateral structure* (lateral form factor, structure factor or the roughness) at surfaces and interfaces in films or multilayers. Thus, the most exhaustive and detailed information on the 3-dimensional structure (transverse and lateral) of multilayers can be gained using a combination of grazing incidence neutron or x-ray scattering techniques, comprising reflectometry and off-specular scattering.

The state of the art in surface preparation and characterisation has made it feasible to produce new types of **materials that are structured on the nanometer scale**. Some of the best examples of engineered solids so far are magnetic multilayers that are developed for reading heads for magnetically-stored data. They consist of sandwiches of magnetic layers separated by a spacer that changes their electrical resistance when exposed to the magnetic field of a stored bit. This effect is termed giant magnetoresistance (GMR) [2,3]. The structures are known as spin valves, since they preferentially transmit electrons of one spin orientation [4,5]. A related phenomenon is oscillatory magnetic coupling, an oscillation in the magnetic orientation of two layers as a function of the thickness of the spacer. Modern scattering depth resolving techniques like polarized neutron reflectometry with off-specular scattering reveal the details of magnetic structures in GMR systems. An example of a Fe/Cr(001) multilayer, showing GMR effect and corresponding experimental data obtained from the experiment on neutron reflectometry [33], is depicted in Figure 1(a).

Recently polarized neutron reflectometry was applied to $VCo_{0.7}Fe_{0.3}$ periodic magnetic stripe array prepared by electron beam lithography and etching techniques [6]. Understanding of magnetic

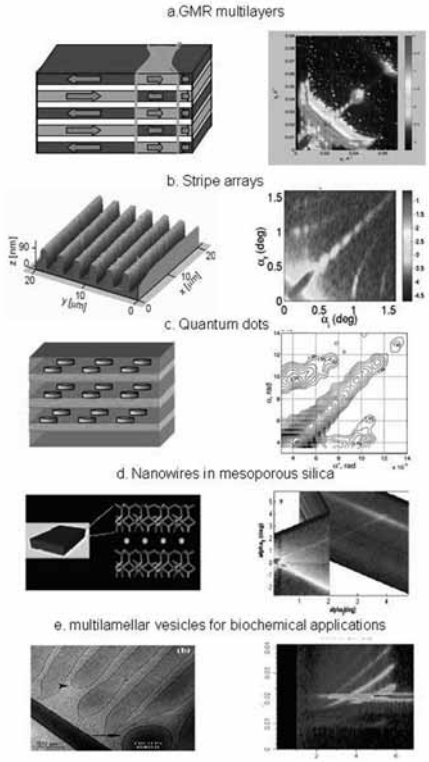

Figure 1. Panels on the left hand side show nanostructures in real space, right hand panels represent the same nanostructures 'as seen' by neutrons in experiments under grazing incidence. a) Fe/Cr multilayer (ML), consisting of magnetic layers (red and rose) with strong in-plane anisotropy and with lateral domains of alternating direction of magnetization (marked with blue arrows) across the film due to exchange coupling via non-magnetic spacer layers (white); 2-dimensional map of intensity reflected and scattered by the Fe/Cr ML. b) Periodic magnetic stripe array with the easy axis along the stripes; 2-D intensity map is determined by the periodic lateral structure, ripple domains and correlations in multidomain ensemble. c) Lattice of Fe dots; scattered intensity is determined by the shape, size, distribution of dots and their magnetization. d) Nano-composite film of metallic nanowires in mesoporous silica matrix; information about the size of the nanowires, monodispersity of their diameter and distribution and orientation within the matrix is encoded in the 2-D intensity map. e) Spherulites, or multilamellar vesicles spontaneously formed in cationic surfactant with low concentration. Complex behavior, phase transition, size of multilamellar vesicles and the details of the transverse and lateral structure of the film can be extracted from the measured reflected and off-specular scattered neutron intensity.

interaction between neighboring stripes is important for magnetoelectronic applications. Magnetization reversal in a stripe pattern with induced uniaxial anisotropy, the domain structure and inter-stripe correlations were successfully obtained using reflection experiment (see example in Figure 1(b)).

Now a days it became possible to produce periodic arrays of submicron dots on flat surfaces or inside of semiconducting, metallic or superconducting films and multilayers used for optical and magnetic storage applications [7,8,9]. One of the first pilot experiments on a lattice of Fe dots with the diameter of 300 nm and height 80 nm was performed with neutrons polarized along the dot magnetization (Figure 1(c)). The magnetization of the dots, their shape, size and periodic distribution averaged over the size of the sample were obtained [10].

Magnetic nanowires embedded in mesoporous silica matrix, being highly organized anisotropic materials, are important nanostructures for development of high density data storage devices. First experiments on neutron scattering were performed to trace the influence of the preparation conditions on magnetic and structural properties of nanowires [11] (Figure 1(d)). From the neutron experiment one can obtain information about the influence of the anisotropy parameters of the magnetic metal and

metal oxide nanowires formed in the structural cavities of solid state nanoreactors (zeolites, mesoporous silica and anodic alumina membranes) on the magnetic properties of the system.

For design of biosensors based on membrane receptors the development of biocompatible interfaces plays an important role [12]. Small unilamellar phospholipid vesicles are basic elements in the design of biophysical model systems for studying the interaction of biomolecules with membrane surfaces [13]. Neutron reflectometry was used to study *in situ* phospholipids bilayer formation [14]. Lamellar vesicles are of particular interest in biochemical field for drug delivery, they can be also used as biological membrane models [15,16]. Recent advances in novel drug delivery systems focused on alternate surfactant systems, which can also produce similar structures [17]. Thus the systems containing mixtures of cationic and anionic surfactants or single-chain nonionic surfactants can form vesicular solutions. The ordered lamellar structure and stability of dichain cationic surfactants was studied by neutron reflectometry [18], the interfacial structure of the aggregates was examined by off-specular scattering (Figure 1(e)).

Although the list of experiments could be continued, already from this brief overview of neutron reflection experiments on nanoscale objects one can see that neutron surface scattering technique is increasingly used in modern centers of excellence for Nanoscience and Nanotechnology development. The reason is that one challenge in the production of nano-size objects is to control their structure, size, shape and symmetry. Using neutron reflectometry one gets access to the structure and morphology of such systems like continuous single and multilayers, periodic lateral structures, buried structures and in contrast to local probes like e.g. transmission electron microscopy or secondary ion mass spectroscopy, it is not destructive and provides information averaged over the whole volume of the system.

2 NEUTRON COHERENCE LENGTH

The information about the three-dimensional structure (transverse and lateral) is encoded in the intensity of neutrons reflected and scattered by the sample. Examples shown in Figure 1 well demonstrate the variety of two-dimensional maps of scattered intensity 'reflecting' the complexity of the investigated objects. Strong intensity, which spreads diagonal (Figure 1 (a)–(d)) or horizontal (Figure 1 (e)) corresponds to the specular reflection. It is determined by the depth profile of the mean scattering length density (SLD), which corresponds to the transverse structure of the system averaged over the whole sample area. The deviations from this averaged structure create *lateral fluctuations of the SLD* around its mean value which give rise to off-specular scattering around the specular reflection.

When do we see off-specular scattering?

It happens when the lateral size of these fluctuations is smaller than the lateral projection of the neutron coherence length. The lateral size of the fluctuations is often described by the *correlation length*. Correlation length is the mean value of the lateral distance between two points, which scatter in phase [19]. In order to estimate the neutron coherence length in the sample position, we will consider the scattering geometry of the reflection experiment. Neutron sources produce non-coherent radiation, so we *do not* discuss the coherence length of the source. Neutron coherence length is determined solely by the time (wavelength) and space (angular) coherence (resolution) of the beam. Perfectly monochromatic point neutron source does not exist, thus the spectral purity (spectral bandwidth) of the source $\delta\lambda/\lambda$ determine the temporal coherence (longitudinal coherence), whereas the angular resolution $\delta\lambda$ (or the size) of the source determine the lateral (transverse) coherence.

2.1 Spectral bandwidth and neutron longitudinal coherence length

Longitudinal coherence length is defined as a distance over which radiation of spectral width $\delta\lambda$ becomes out of phase by π, as shown in Figure 2. For a wavelength λ propagating with n periods longitudinal coherence length is

$$L_l = \lambda n \tag{2.1}$$

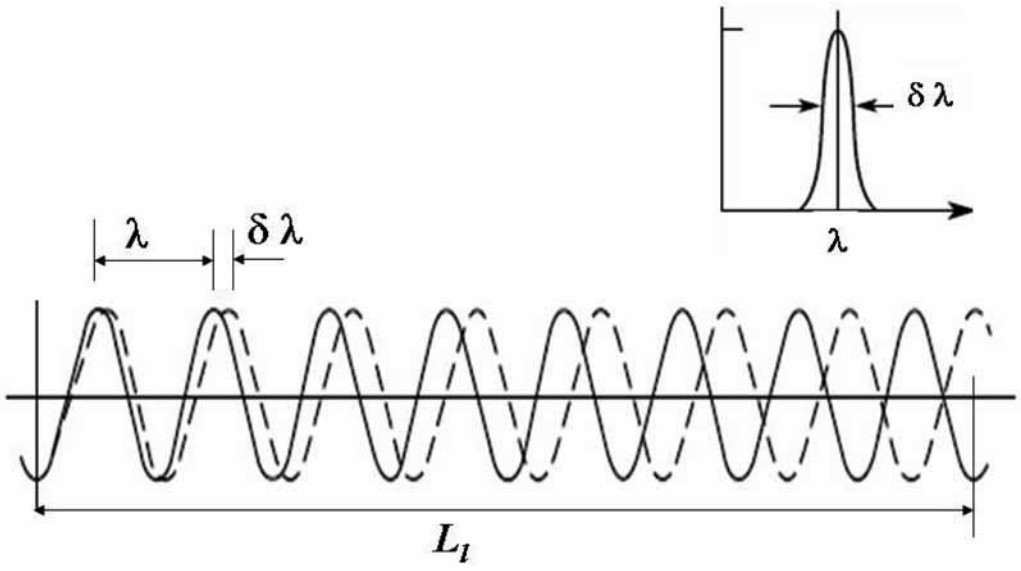

Figure 2. Longitudinal (temporal) coherence length. It is a distance neutron travels within coherence time and determines the maximum depth of the object in a reflection experiment.

For a wavelength $\lambda + \delta\lambda$

$$L_l = (\lambda + \delta\lambda)\left(n - \frac{1}{2}\right) \tag{2.2}$$

From Eq.(2.1) and Eq.(2.2)one can easily obtain the expression for the longitudinal coherence length in the following form

$$L_l = \frac{\lambda^2}{2\delta\lambda} \tag{2.3}$$

The longitudinal coherence length defines the largest path difference for which interference is possible. From easy estimation one can obtain that in the neutron reflection experiment the path difference between waves reflected from the surface and the substrate is normally smaller than the L_l.

2.2 Angular resolution and neutron lateral coherence length

From the Heisenberg's uncertainty principle follows that the neutron momentum becomes undefined as the position in the aperture becomes more and more well-defined.

The point source does not exist, therefore the angular resolution has a finite value. The angular resolution determines the lateral neutron coherence length. From each point of the sample one sees the source (or a collimator, which determines the resolution) of size a on distance R within the divergence angle ϕ_i. Normally $R >> a$. From geometrical consideration (Figure 3) follows, that the lateral coherence length L_s (the coherence length across the beam) can be found as

$$L_s = \lambda\frac{D}{2a} = \frac{\lambda}{2\phi} = \frac{\lambda}{\delta\alpha} \tag{2.4}$$

where $\delta\alpha$ is the angular resolution.

For the small angles of incidence α one should take into account the projections of both coherence lengths on the sample surface, so that

$$L_l^{\alpha} = \frac{L_l}{\cos\alpha} = \frac{\lambda^2}{2\alpha\delta\lambda}$$

$$L_s^\alpha = \frac{L_s}{\sin\alpha} = \frac{L_s}{\alpha} = \frac{\lambda}{\alpha\delta\alpha} \tag{2.5}$$

During the reflectometry experiment the projection of the lateral coherence length is not a constant and can change by factor 10–15. For the monochromatic beam it changes with the scanning of the incident angle. For the time-of-flight experiment at a fixed incident angle L_s^α is a function of the neutron wavelength.

The same considerations stand for the coherence length determined by the spatial detector resolution and the distance samples-detector, so that for the determination of the resulting coherence length one should take into account the incident beam and scattered beam parts.

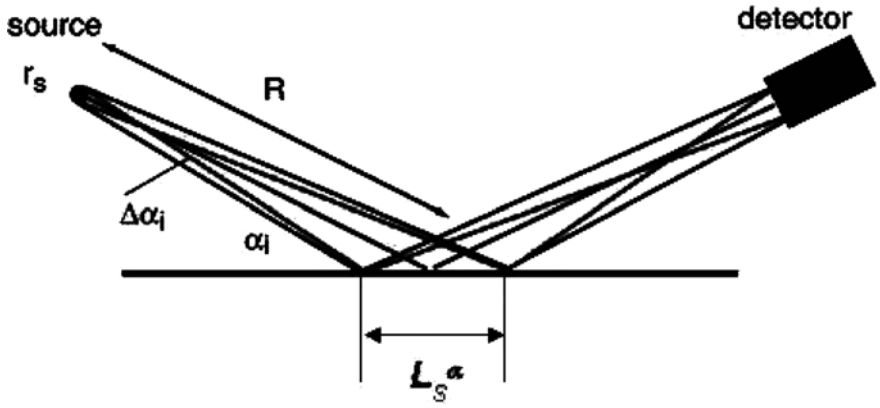

Figure 3. Spatial neutron coherence length L_s^α in the sample position. R is a distance from the source with linear dimensions r_s, α is the angle of incidence, $\Delta\alpha$ is the angular divergence.

From a simple estimation one finds that the L_s^α can be as large as a few hundreds of microns along the beam. Hence, the transverse coherence length in the film plane is large compare to the length scales of the lateral extension of 'nanos-scale' structures or inhomogeneities, but small compare to the lateral sample size. Thus, the scattered radiation is the incoherent sum of the contributions, scattered from statistically independent parts of the film.

3 SCATTERING UNDER GRAZING INCIDENCE AND DISTORTED WAVE BORN APPROXIMATION

Traditionally in diffraction experiment the scattering of neutrons is calculated within the Born approximation combined with the Fermi pseudopotential, which is parameterized by the atomic scattering length. In this approximation a plane wave scattered by a weak scatterer, is not much perturbed by the scattering process. This approximation gives rather accurate answers being applied to neutron diffraction or small angle scattering, when the most of the neutrons are not deviated by the scattering process. However, for the reflection experiment, especially close to the total reflection region, only a small part of the neutrons is transmitted and the most of the incident beam is reflected.

A more appropriate way of making the perturbation calculation for reflectometry is to find first exact wave functions for the neutron interacting with the mean film potential averaged over the lateral coordinate $\boldsymbol{\rho}$. To calculate the off-specular scattering, one should make a perturbation calculation using the found wave functions and a perturbation potential, which is the deviation from the mean film potential. This perturbation theory is known as distorted wave Born approximation (DWBA) [20]. In a pioneer work of Vineyard [21] it was first applied to the case of the grazing incidence surface diffraction and shortly after to the study of the structure of the liquid-vapor interface of a liquid metal [22]. Later, Sinha

et al. [23] and R. Pynn [24] used DWBA approach for a calculation of the specular and diffuse scattering from rough surfaces. The routine was developed further for the calculation of the magnetic [25] and non-magnetic [26] off-specular scattering based on the super-matrix formalism [27].

3.1 Specular reflection

Let us consider a simple reflectometry experiment (Figure 4). Incident neutrons of wavevector $\mathbf{k_i}$ are specularly reflected to wavevector $\mathbf{k_f}$. In this case the incident angle α_i is equal to grazing angle of reflection α_f. If at the scale smaller than the projection of the neutron coherence length L_s^α the variation of the interaction potential is a function of only z-coordinate perpendicular to the sample surface $V_0(z)$, the interfaces can be regarded as laterally flat. Then the solution of the Schrödinger equation

$$\{\nabla^2 + k_0^2 - (2m/\hbar^2)V_0(z)\}\,|\mathbf{\Psi}(\mathbf{r})\rangle = 0 \tag{3.1}$$

above the surface can be written as

$$|\mathbf{\Psi}(\mathbf{r})\rangle = \exp(i\boldsymbol{\kappa}\boldsymbol{\rho})\{e^{ip_i z} + \hat{R}e^{-ip_i z}\}\,|\psi(0)\rangle = 0 \tag{3.2}$$

where $\mathbf{k} = \{\hat{\mathrm{e}}, p\}$ is the neutron wave vector and $k = 2\pi/\lambda$, $\boldsymbol{\kappa}$ is its lateral, and p_i is its normal to the surface components. $|\mathbf{\Psi}(\mathbf{r})\rangle$ is two-component vector of spin states, $\hat{R}$ is the reflectance matrix. Inside the film the wave field is formed by the waves transmitted trough and reflected from each interface.

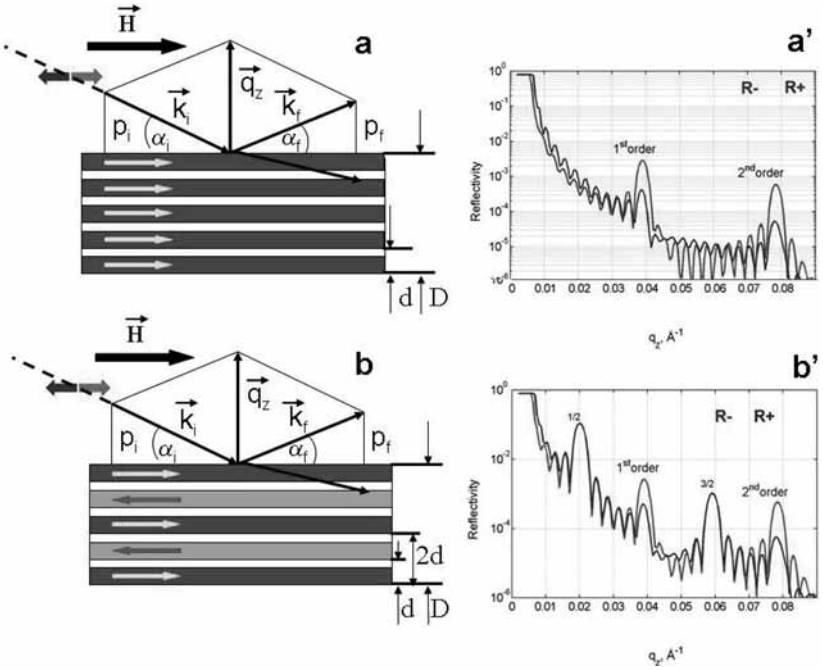

Figure 4. Scheme of a reflectometry experiment. (a) Magnetic ML (with repeating bilayers of a thickness d resulting in a total thickness D) in a saturating external magnetic field $\boldsymbol{H}$; $\boldsymbol{k}_i$ and $\boldsymbol{k}_f$ are the wave vectors of a neutron incident with an angle α_i and specular reflected under the angle α_f. (a') Calculated R^+ and R^- reflectivity profiles as a function of momentum transfer q_z; positions of the Bragg peaks are determined by the bilayer thickness d, the Kiessig fringes [30] are due to the total film thickness D. (b) ML in a remanent external magnetic field resulting in the opposite alignment of the magnetization vectors in the alternating magnetic layers. (b') Calculated R^+ and R^- reflectivity profiles have $1/2$ and $3/2$ - order Bragg peaks additional to ones in Figure 4(a'), they are determined by the doubling of the 5 magnetic part of the scattering length density profile.

Transmission $\hat{t}$ and reflection $\hat{r}$ operators can be found from the boundary conditions and the vector of spin states transforms into

$$|\psi(z)\rangle = \hat{t}e^{i\hat{p}z} + \hat{r}e^{-i\hat{p}z} \tag{3.3}$$

For magnetic media the mean magnetic field is $\mathbf{B} = \mathbf{H} + 4\pi\mathbf{M}$, where $\mathbf{H}$ is the external magnetic field and $\mathbf{M}$ is the mean in-plane magnetization. The quantization axis is along the vector $\mathbf{B}$, thus the eigenvalues of the operator $\hat{p}$ are written as

$$p^{\pm} = (p_i^2 - p_N^2 \mp p_M^2)^{1/2} \tag{3.4}$$

with $p_N = \sqrt{4\pi n b_N}$ and $p_M = \sqrt{2m\boldsymbol{\mu}\mathbf{B}}$, where nb_N is the nuclear scattering length density, $\boldsymbol{\mu}$ is neutron magnetic moment. From the continuity conditions for the wave functions and their first derivatives at each interface of a multilayer structure with a set of layers with thickness d_n follow equations

$$\hat{t}_n e^{ip_n d_n} + \hat{r}_n e^{-ip_n d_n} = \hat{t}_{n+1} + \hat{r}_{n+1}$$

$$(\hat{t}_n e^{ip_n d_n} - \hat{r}_n e^{-ip_n d_n})\hat{p}_n = (\hat{t}_{n+1} - \hat{r}_{n+1})\hat{p}_{n+1} \tag{3.5}$$

A solution of these equations can be found via the supermatrix formalism [27] as well as via the iteratively exact method called Parrat's recursion relation [28].

An example of calculated reflectivity curves from a magnetic multilayer with flat interfaces is shown in Figure 4. The system is a 'typical' multilayer structure, showing GMR effect.

It is composed from twelve identical Fe magnetic layers with uniaxial in-plane anisotropy separated by non-magnetic Cr spacers and deposited on a Si substrate. The direction of the external magnetic field is chosen along the easy axis. In saturation (Figures 4(a), 4(a')) the layer magnetizations are fully magnetized parallel to the external field. In this case only non-spin-flip (NSF) reflectivity curves, R^{++} and R^{--} exist, which correspond to two orientations of neutron polarization. The reflectivity curves have well known characteristic features, like the oscillations determined by the total thickness D and the Bragg peaks, corresponding to the bi-layer thickness d.

When the external magnetic field is released down to a small value of a guide field, the magnetizations in alternating Fe layers will align anti-parallel to each other due to the exchange-coupling interaction [29]. This will manifest in the appearance of additional $1/2$, $3/2$, etc. -order Bragg peaks (see Figure 4(b')), corresponding to a doubling of the bi-layer structure due to the magnetic term in Eq.(3.4). The calculations shown in (Figure 4(b')) are valid only for the case of a monodomain state of each magnetic layer.

However, it would be difficult to imagine that in the latter case the magnetic layers of the discussed multilayer system will preserve a monodomain state in remanence [31]. In order to minimize the free energy of the ferromagnetic material, the magnetic layers will decompose into a set of domains with opposite magnetization, which coincide with a direction of easy magnetization axis. In this case two scenarios are possible: large and small domains.

The first scenario is when the domain size is greater than L_s^{α}. This conjecture can be proven by the absence of off-specular scattering. If it is so, one should calculate reflectivity profiles for each type of domains and add them afterwards incoherently.

The second scenario is if a certain amount of off-specular scattering is detected. It means that the lateral magnetic inhomogeneities (magnetic domains) are smaller than L_s^{α}, then the wave is not only reflected in specular direction and transmitted in the direction of the incident beam, but also scattered in off-specular direction both above and below the horizon (Figure 5). This case should be treated within the DWBA formalism and will be discussed in the next section.

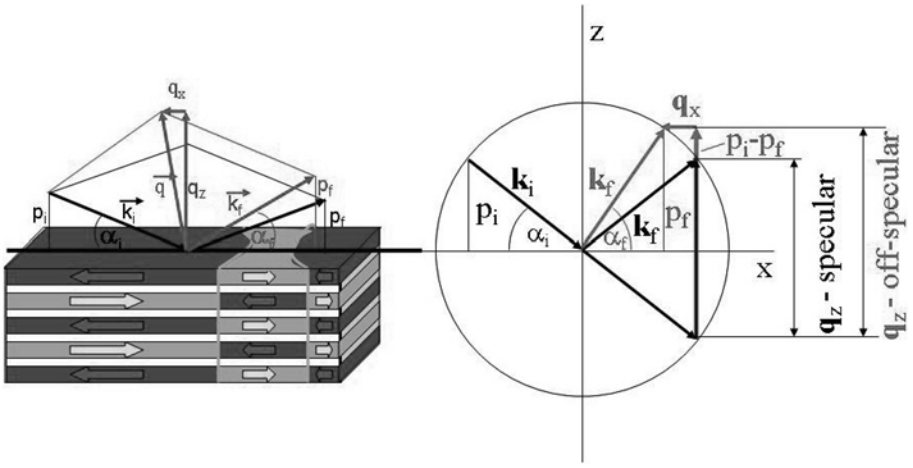

Figure 5. Magnetic ML with magnetic domains. Incident $\boldsymbol{k}_i$ and specular reflected $\boldsymbol{k}_f$ wave vectors are shown with black arrows, arrows marked with red color correspond to off-specular scattered wave. Diagram on the right hand side represents the scattering process in the reciprocal space.

3.2 Off-specular scattering

Lateral fluctuation of the SLD around its mean value give rise to the perturbation interaction potential operator in the spin space

$$\hat{V}_p(\mathbf{r}) = \hat{V}(\mathbf{r}) - \hat{V}_0(z) \tag{3.6}$$

The wave functions $\psi(\mathbf{k}_i; \boldsymbol{\rho}, z)$ and $\psi(\mathbf{k}_f; \boldsymbol{\rho}, z)$ of incident and scattered waves for mean film potential averaged over the lateral coordinate $\boldsymbol{\rho}$ were determined in the previous section. Using these wave functions and the scattering, we find then the scattering amplitude

$$\hat{f}(\mathbf{k}^f, \mathbf{k}^i) = -\frac{m}{2\pi\hbar^2} \int d\mathbf{r} \left\langle \psi^f(k^f, \boldsymbol{r}) \right| \hat{V}_s(\mathbf{r}) \left| \psi^i(k^i, \boldsymbol{r}) \right\rangle \tag{3.7}$$

The perturbation potential is proportional to the scattering length density of the fluctuation $\hat{F}(Q)$, which can be written [25] as

$$\hat{F}(Q) = b_N F_N(\mathbf{Q}) + (\boldsymbol{\sigma}\boldsymbol{m}_\perp) b_M F_M(\mathbf{Q}) \tag{3.8}$$

where b_N and b_M are the nuclear and magnetic scattering lengths, $F_N(\mathbf{Q})$ is the nuclear structure factor,$F_M(\mathbf{Q})$ is the magnetic form factor, $\boldsymbol{\sigma}$ is the vector of the Pauli matrices, $\boldsymbol{m}_\perp$ is the component of the layer magnetization vector perpendicular to the momentum transfer.

For a multilayer structure one should take into account refraction and the scattering of waves reflected from each interface. This was done in the frame of the DWBA in [25,26,27,28,29,30,31,32] and the scattering operator for each layer looks as follows:

$$\hat{F}_{fi} = \hat{t}_f \hat{F}^{tt} \hat{t}_i + \hat{t}_f \hat{F}^{tr} \hat{r}_i + \hat{r}_f \hat{F}^{rt} \hat{t}_i + \hat{r}_f \hat{F}^{rr} \hat{r}_i \tag{3.9}$$

The important point is that the scattering from a magnetic layer is accompanied with transition between the spin states $\{+, -\}$. From the general definition [32] the scattering cross section and the reflectivity can be written

$$\frac{d\sigma}{d\Omega} = Tr\{\hat{\rho}^i (\hat{F}^+_{fi}) \hat{\rho}^f \hat{F}_{fi}\} \qquad\qquad R = Tr\{\hat{\rho}^i (\hat{R}^+) \hat{\rho}^f \hat{R}\} \tag{3.10}$$

where the density matrices $\hat{\rho}^i$ and $\hat{\rho}^f$ describe the properties of polarizer and analyzer, respectively

$$\hat{\rho}^i = \frac{1}{2}(1 + \boldsymbol{\sigma}\boldsymbol{P}_i) \qquad \hat{\rho}^f = \frac{1}{2}(1 + \boldsymbol{\sigma}\boldsymbol{P}_f) \tag{3.11}$$

Substitution of the Eq.(3.9) into Eq.(3.10) provides a general equation for the scattering cross sections [27], whose diagonal elements are written as follows [32]

$$\frac{d\sigma^{yy}}{d\Omega_{++}} = \frac{d\sigma^{yy}}{d\Omega_{--}} = 0 \tag{3.12}$$

$$\frac{d\sigma^{yy}}{d\Omega_{+-}} = \left|F_x - iF_z\right|^2 \tag{3.13}$$

$$\frac{d\sigma^{yy}}{d\Omega_{-+}} = \left|F_x + iF_z\right|^2 \tag{3.14}$$

$$\frac{d\sigma^{xx(zz)}}{d\Omega_{++}} = \frac{d\sigma^{xx(zz)}}{d\Omega_{--}} = \left|F_{x(z)}\right|^2 \tag{3.15}$$

$$\frac{d\sigma^{xx(zz)}}{d\Omega_{+-}} = \frac{d\sigma^{xx(zz)}}{d\Omega_{-+}} = \left|F_{z(x)}\right|^2 \tag{3.16}$$

The application of obtained formulas to different magnetic and non-magnetic structures allows for analysis of specular reflectivity and off-specular scattering from layered systems. This will be shown in the next sections.

4 NUMERICAL CALCULATIONS: EXAMPLES

The various experimental data shown in Figure 1 are collected in the broad range of incident and scattered momentum transfers, including the total reflection region. What are the sources of off-specular scattering? One can classify several main groups, which are shown in Figure 6 and which embrace the majority of possible 'layer fluctuations'.

The first one is the interfacial (surface) roughness (see Figure 6(a)). Roughness consists of surface irregularities which result from the various processes. These irregularities combine to form surface texture. Usually roughness is characterized by the absence of the regular lateral structure and is treated in terms of its correlation properties on the mesoscopic (sub-micrometer) scale using some distribution functions.

Nanoparticles embedded in a matrix, as shown in (Figure 6(b)), change the morphology and can initiate a phase transformation of the host matrix. Lateral fluctuations in such system will be characteraized by the particle form factor and the particles' size distribution. The lateral fluctuations from the nano-objects inside the layers produce off-specular scattering *additional* to the one from the interfaces.

Domain formation plays a crucial role in the magnetization – reversal characteristics. Except the case of the saturating external field, the lateral magnetic structure in films and multilayers is not stable and falls into a set of lateral domains (see Figure 6(c)). The magnetic scattering cross section is determined by the domain lateral form factor, the multilayer structure factor and a combination of reflectance and transmittance amplitudes for both spin states. The off-specular scattering carries the information *not only on domains*, but also on mean magnetization averaged over domains [33].

Lateral (surface or buried) periodically patterned structures like arrays of micron and submicron size stripes, dots, rings etc., which found application in optical and magnetic storage devices, are shown in (Figure 6(d)). The off-specular scattering from such structures is determined by the form factor and the internal structure of the lateral objects, as well as by their structure factor.

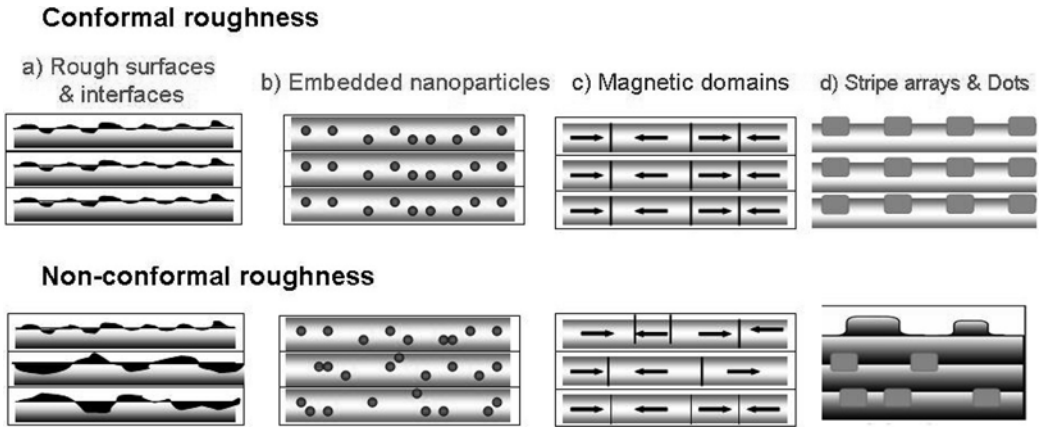

Figure 6. Different types of the layer density fluctuations (or 'roughness') in films and multilayers. The sketches in the top and bottom rows show examples of two limiting cases of ideally conformal and non conformal roughness.

An important parameter in the description of the lateral surface and interfacial structure is the *parameter of conformity*. This is a measure of the replication of the roughness profile from interface to interface (or from layer to layer) within a multilayer. The sketches in the top and bottom rows in Figure 6 show examples of two limiting cases of ideally conformal and non conformal systems.

In the following we will discuss and illustrate different effects in off-specular scattering pattern.

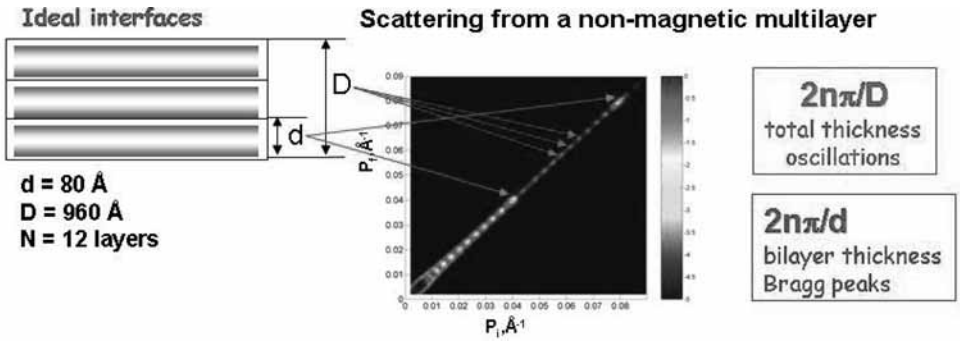

Figure 7. 2D intensity map from a non magnetic ML with ideal interfaces. The strong intensity along the diagonal corresponds to the specular reflection, total reflection region is near the origin of the map, followed by the total thickness oscillations and the two Bragg peaks originating from the bilayer thickness d.

Let's start from a simplest case of a multilayer structure with ideal interfaces (see Figure 7). The structure of the film is chosen to be the twelve times repeated bi-layer thickness d, resulting in the total film thickness D. In the absence of roughness only the specularly reflected intensity determined by the transverse structure of the film will be obtained. The result of the calculation is shown on the right side of the Figure 7. It is presented in a form of a two-dimensional map as a function of p_i and p_f, the normal components of the neutron wave vector ($p_i = k \sin \alpha_i$ and $p_f = k \sin \alpha_f$, where α_{if} are the glancing angles of incidence or scattering, respectively, as explained in Figure 4). The main features of specular reflectivity are the oscillations, determined by the vertical periodicity of the SLD in the film. The specular reflected intensity along the line $p_i = p_f$ shows the total thickness oscillations with period $p_i + p_f = 2\pi/D$, as well as the 1^{st} and 2^{nd} order Bragg peaks at $p_i + p_f = 2\pi n/d$. The total reflection region is visible as high intensity close to the origin.

If within the L_s^α the interfaces in the multilayer are not flat and the transitional invariance in lateral directions are violated, then the roughness induced local fluctuations of an actual SLD around its mean value give rise to the off-specular scattering. Figure 8 shows the calculation of the same multilayer as in Figure 7, but with rough conformal interfaces. The lateral and transverse dimensions of roughness are $\xi = 30$ nm and $\sigma = 0.5$ nm. The significant feature of conformal roughness is that the scattering is arranged into the sheets stretched perpendicular to the specular line. There are two types of the off-specular scattered intensity. The first one corresponds to the scattering arranged along the lines $(p_i + p_f) = 2\pi N/D$ running through the thickness oscillations on the reflectivity line. They appear due to conformity between the substrate and surface roughness. The second one is arranged into the Bragg sheets stretched along the lines $(p_i + p_f) = 2\pi n/d$ crossing the Bragg peaks on the reflectivity ridge. Off-specular sheets are distorted due to refraction effects at low values of p_i and/or p_f approaching the total reflection region and become straight at high values of p_i and p_f.

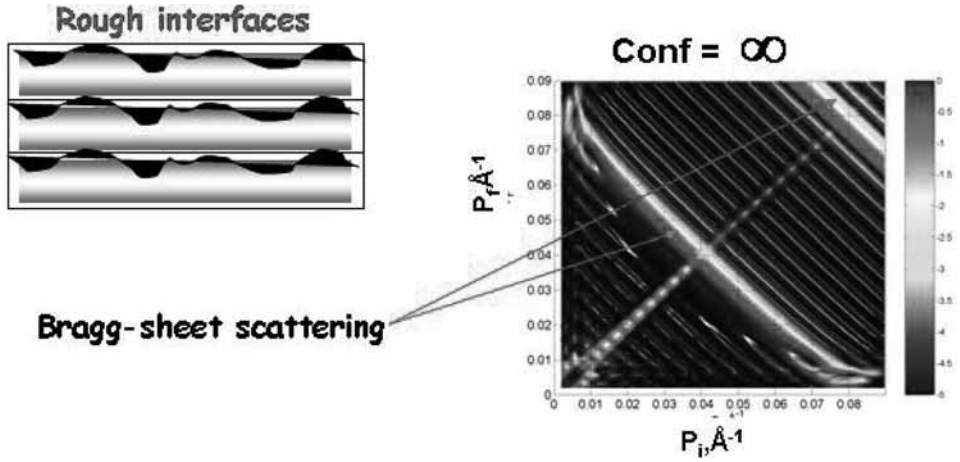

Figure 8. 2D intensity map from a non magnetic ML with conformal interfacial roughness. Off-specular scattering is arranged into the sheets crossing the reflectivity line in the positions of the thickness oscillations (lower intensity) and of the Bragg peaks (marked with arrows).

Until now we have considered a non-magnetic system. However, as it was already discussed above, magnetic films and multilayers in addition to non-magnetic interfacial roughness can form a domain structure and/or interfacial magnetic roughness, which give rise to magnetic off-specular scattering.

Let us consider now the scattering from a magnetic multilayer. For simplicity we suppose first, that the interfaces are flat within L_s^α. The system, which we model and calculate, is shown in the Figure 9. It consists of twelve bilayers ^{57}Fe(70Å)Cr(10Å)] with in-plane four-fold anisotropy and grown on Al_2O_3 substrate. This is an excellent example of a system showing giant magneto-resistance effect [2,3] related to antiferromagnetc exchange coupling interaction between the magnetic moments in alternating Fe layers and with their mutual reorientation under an applied magnetic field [33]. The external magnetic filed **H** is applied parallel to the sample surface. For $H < H_{saturation}$ the sample falls into lateral domains sketched in Figures 9(a) and 9(b). For simplicity we assume a homogeneously canted state in the layer magnetization distribution with the canting angles $\pm\varphi$. Domains reduce the dipolar energy via demagnetization of each individual layer *n*, and the mean value of magnetization is $\overline{M}_n^\perp = M\overline{\sin\varphi_n}$.

An example of numerical results simulating the described model of reflected and scattered intensity for incoming neutrons in '-' and '+' states are shown in Figure 9(d), 9(e) for the case when magnetic domains with mean size of 280 nm are conformal through the multilayer stack. Two dimensional plots reveal a number of remarkable features. One can clearly see two antiferromagnetic Bragg sheets along the lines $(p_\pm^i + p_\mp^f)d \approx \pi, 3\pi$, and a set of low intensity sheets running parallel to the Bragg sheets. The

distance between them is determined by the total thickness of the multilayer. The other important feature is that the off-specular intensity is strongly asymmetric. This effect is determined by the asymmetry in the spin-flip scattering amplitude F_z with respect to interchange of the incident and outgoing wave numbers [32]. The critical values at which the off-specular scattering is cut, are related to the scattering length densities Nb being different for the two neutron spin states: $Nb^{\pm} = Nb_n \pm Nb_m$, where N is the atomic number density, b_n and b_m are the nuclear and magnetic parts of the scattering length, respectively [34]. The spin-flip off-specular scattering is determined by the perpendicular component of the magnetization vector.

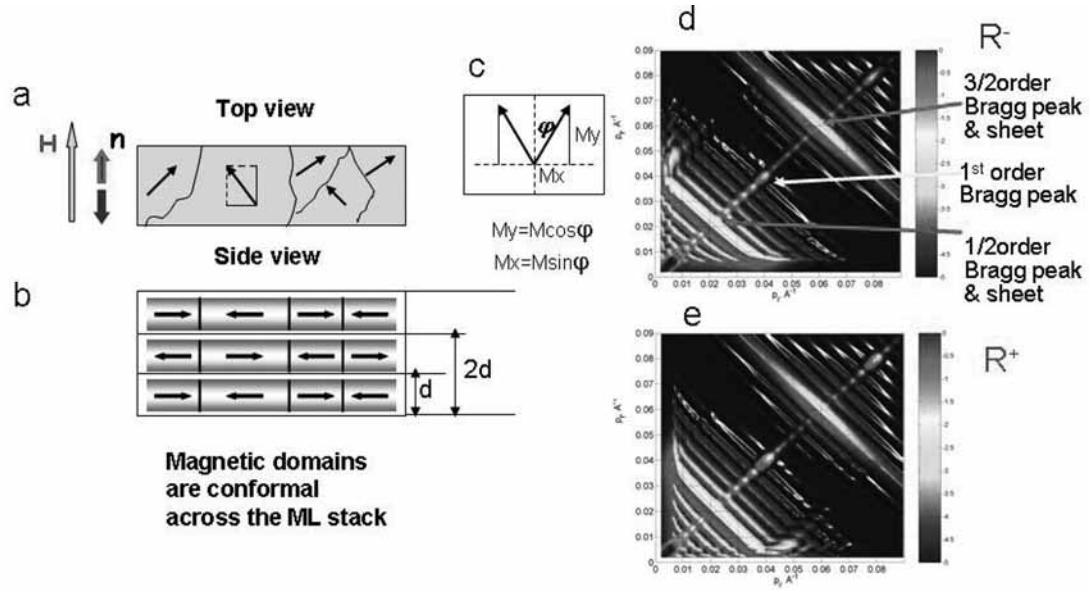

Figure 9. Scattering from a magnetic ML with ideal interfaces and magnetic domains. Lateral and transverse structure of the system is shown in panels a (top view) and b (side view). c) Directions of the magnetization vectors in two types of domains with a canting angle φ with respect to the neutron quantization axis. 2D maps of reflected and scattered intensities for neutrons with spin anti-parallel (d) and parallel (e) to the external magnetic field. The strong asymmetry in the off-specular scattering is due to the spin-flip origin of the scattering and two critical values of the scattering length density for two neutron spin states.

The other effect seen in Figures 9(d), 9(e) is the appearance of 'anomalous' Bragg sheets. They spread parallel to the reflectivity ridge on a distance $(p_i^+ - p_f^+)D \approx \pi$ [35]. This type of scattering appears when the scattered neutron wave is reflected by the interface. Again, due to the spin-flip origin of the scattering in the present example it is strongly asymmetric.

Now we will combine the two cases in a rather complicated system of a multilayer with rough interfaces and magnetic domains in the magnetic layers. This system is shown in Figure 10. The two-dimensional pattern of the scattered intensity for spin-down neutrons is a superposition of spin-flip and non-spin flip off-specular scattering, originating from the two sources of non-magnetic interfacial roughness and magnetic columnar domains as it was discussed earlier. This example shows that off-specular scattering is roughness selective, thus the different parts of the pattern are determined by different processes and can be analyzed in the experiment [33,34,35].

The appearance of characteristic features in the off-specular pattern depends not only on the lateral fluctuations of SLD but also on their vertical correlation (or conformity parameter). Until now we considered the case of ideally conformal roughness with full replication from interface to interface or from

layer to layer. If the roughness profile of different interfaces correlates only partially on a distance of vertical correlation length $\Lambda_\perp$, then one should introduce an inter plane correlation function [36]

$$\frac{d\sigma}{d\Omega} = e^{-|z_m - z_n|/\Lambda_\perp} \sum_{l,l'=1} Tr(\rho^i \tilde{F}^+_{l'} \rho^f \tilde{F}_{l'}) \tag{4.1}$$

where $\tilde{F}_{l'}$ is the scattering operator, $\rho^{i,f}$ are the density matrices and z is the transverse coordinate. Figures 10(b) and 10(c) show calculations of off-specular scattering for the same system as in Figure 10(a), but assuming different degree of conformity. In the case shown in Figure 10(b) the SLD fluctuations (magnetic and/or non magnetic) are partially correlated from layer to layer, e.g. the phases of scattered waves are partially coherent. In this case in addition to the sheet-scattering from correlated roughness an additional intensity from not-correlated roughness, so called Yoneda scattering, appears and spreads along the lines $p^{i,f} = p^c$.

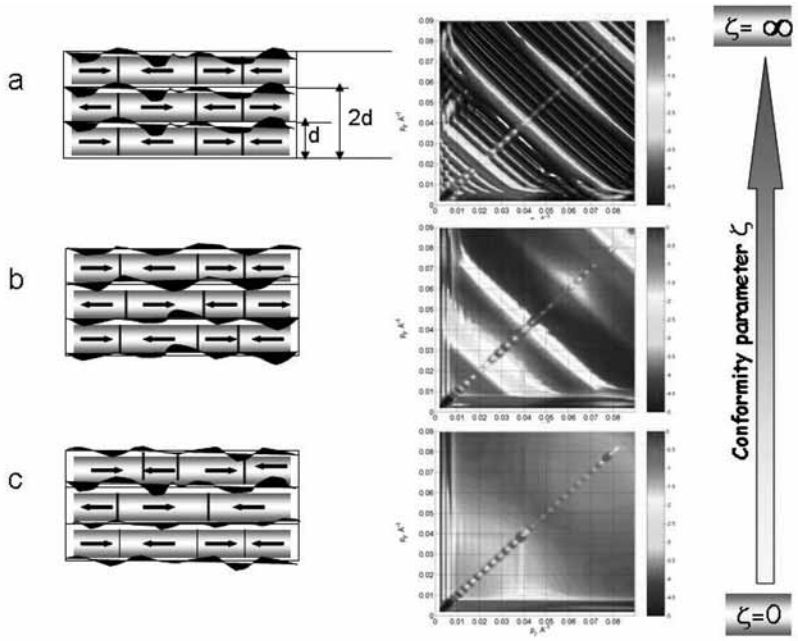

Figure 10. Scattering from magnetic multilayer with rough interfaces and magnetic domain structure. Left panels (from top to bottom) show in real space MLs with the same structure but with different conformity between the interfacial roughness and between the magnetic domains: a) ideally conformal system; b) ML with partial degree of conformity; c) system with non-conformal magnetic and non magnetic fluctuations. The panels on the right side represent 2D intensity maps calculated from the MLs with different parameter of conformity ζ.

The last case (see Figure 10(c)) corresponds to the system with non correlated roughness when interfaces scatter independently. The Bragg sheet scattering disappears, the off-specular scattering from individual interfaces is superimposed, and the Yoneda scattering becomes more intensive. The remarkable feature is that the Yoneda scattering from this system is rather complicated. The asymmetric part the Yoneda scattering is the spin-flip intensity from non correlated magnetic domains and the symmetric part is determined by the non correlated non magnetic interfacial roughness.

In the numerically calculated examples described above we have shown and explained the main features appearing in different patterns of off-specular intensity scattered by magnetic and non magnetic systems. In the next section we will discuss several experimental results.

5 EXPERIMENTAL DATA: EXAMPLES

5.1 Self-assembled copolymer mulilayers

In view of current interest in fundamental problems of polymer surface and interface formation, as well as due to technological importance, the structures of diblock multilayers were intensively studied by employing a number of different experimental techniques such as optical and atomic force microscopy, transmission electron microscopy, X-rays and neutron specular reflectometry. However, none of them gives detailed quantitative information simultaneously on both outer-layer lateral arrangement and the transverse and lateral structure of the inner interfaces. This information can be obtained from the experiments on off-specular neutron scattering, inasmuch as the different contributions to the measured pattern are discerned and modeled [26,36].

Symmetric diblock copolymers consisting of two chemically different polymer chains linked end to end are micro-phase separated into domains due to the immiscibility of the two polymers. The mixture of this diblock copolymer with a solvent is spin coated onto a flat substrate. During the following slow annealing to above the glass transition temperature the micro-phase separation leads to a lamellar ordering parallel to the substrate.

An uncompleted top layer and rough interfaces are characteristics for most symmetric diblock-copolymer polymer films after annealing. The surface consisting of islands, holes or 'labyrinth'-type structures together with interfacial roughness buried inside the multilayer film, create off-specular scattering. Using a model based on the dynamical scattering theory for the analysis of the 2-dimensional map of the scattered intensity, we identified and modeled the different sources of off-specular scattering and obtained rather complete information on the surface topology and the morphology of the interface roughness.

The system under consideration is a thin film of a symmetric diblock copolymer of deuterated polystyrene, d-PS, and polybuthylmethacrylate, PBMA, denoted P(d-S-b-BMA) with the molecular weight $Mw = 248300$ g/mol, polydispersity $Mw/Mn = 1.03$ and a symmetric block ratio $(f = 0.5)$. The sample was prepared by spin coating a toluene solution of the copolymer blend onto the glass substrate and annealed at temperature 151°C for 94 hours.

The reflected and scattered intensity is depicted in Figure 11(a) as a function of p_i and p_f . The specular reflection runs along the ridge $p_i = p_f$. It is evident that the axis $(p_i + p_f) = Q_z$ represents the usual perpendicular momentum transfer in specular reflection. The off-specular scattering described as a function of $(p_i - p_f)$ spreads out left and right from the specular ridge. The model fit to the data shown in Figure 11(b) reproduces the measured intensity distribution. The model itself is schematically depicted in Figure 11(c). The details of the model are discussed in the following.

The fit to the reflectivity line reveals that the polymer film consists of 4 complete layers of P(d-S-b-BMA) and a top layer with holes. The reduced SLD of the top layer reflects the presence of holes covering **10%** of the film surface area. The following sequence of Bragg-peak positions is defined by the thickness L of the PS-PBMA multilayer and the intensity distribution of the Bragg peaks by the SLD amplitudes above the substrate. The value of L varies slightly across the film thickness. The interfaces are modeled by error functions, the width of which represents its roughness.

The obtained SLD (or potential) structure enters into the wave equation to obtain the "zero order" solution of the scattering process. Here we introduce not the potential with sharp interfaces [23] but the laterally averaged potential.

In order to distinguish between the effects of roughness and islands, one needs to figure out which particular features in Figure 11 originate from each of them.

The model calculation for the roughness at the interfaces yields the picture in Figure 12(a), 12(a') containing contributions from conformal and non-conformal roughness. The vertical correlation length expressed by the conformity parameter, which in terms of number of interfaces determines the width of the correlation, gives the ratio between the two scattering mechanisms. Here the best agreement is found with a conformity parameter of 6.

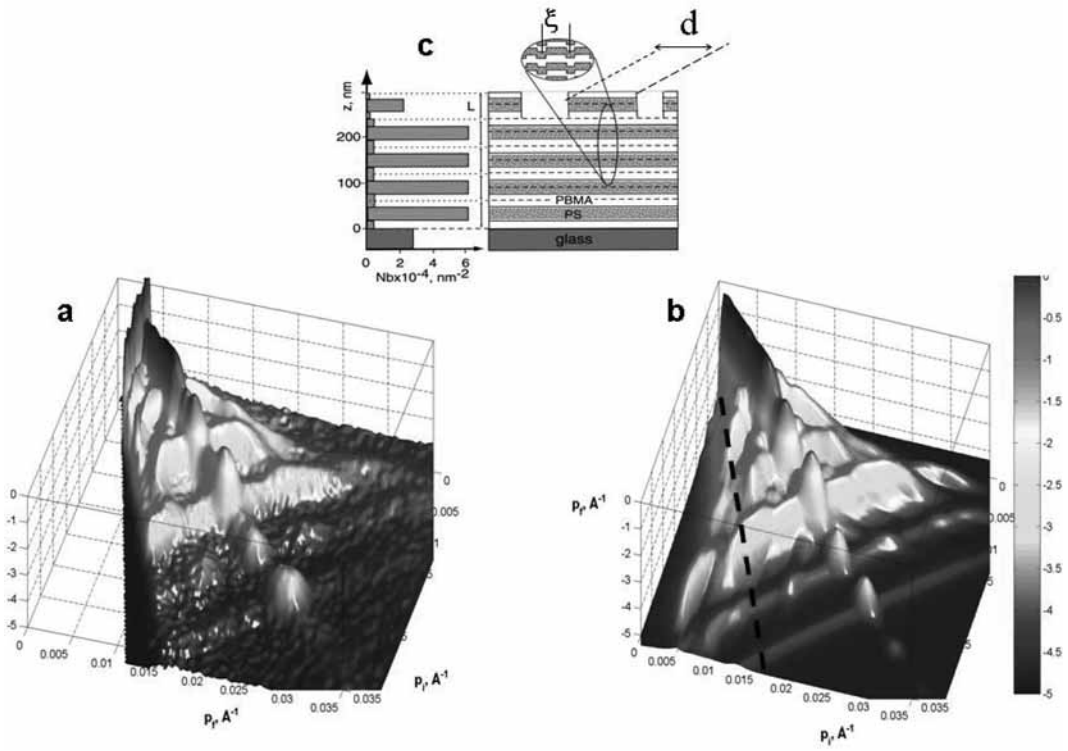

Figure 11. Experimentally mesured (a) and theoretically modeled (b) three-dimensional intensity maps of specular reflection and off-specular scattering from the annealed sample of P(d-S-b-BMA) multilayer film. (c) Neutron scattering length density profile of the transverse structure of the ML as function of the distance from the substrate extracted from the model fit to the data; (d) lateral structure of the ML shows the lateral interfacial roughness fluctuations with the mean lateral distance ξ, as well as the surface island structure with the mean lateral dimension d.

The significant feature of conformal roughness is Bragg-sheet scattering through the n Bragg-peaks on the reflectivity line with proportional intensity to them and extending along $(p_i + p_f)_{nBragg}$. Deviations from this behavior become apparent whenever the Bragg-sheet scattering crosses with events arising from dynamical scattering as Yoneda scattering or anomalous Bragg-sheet scattering. The Yoneda and super-Yoneda scattering is just non-conformal roughness scattering, running out of the critical edge (along $p_{i,f} = p_c$) and Bragg-peaks (with p_i or $p_f = (p_{i,f})_{nBragg}$), respectively. The advantage of the plot in $(p_i + p_f) = f(p_i - p_f)$ is that $(p_i - p_f)$ is a linear function of α_i and α_f the incoming and outgoing scattering angle, whereas Q_x the lateral momentum transfer, is a non-linear function of these angles. Therefore the Yoneda scattering appears here as straight lines. However, also the Yoneda scattering is affected by the crossing with the Bragg-sheet scattering and the anomalous Bragg-sheet scattering. The latter is parallel to the reflectivity line along the lines with $(p_i - p_f) = 2np/L$. Peaks appear if one of the intersecting Bragg sheets is suppressed while the other is enhanced by the structure factor. Otherwise the interference between "normal" and "anomalous" scattering is destructive. Apart from these details the overall intensity distribution along the Bragg sheets mostly depends on the lateral correlation length ξ and fractional exponent ν of the roughness height-height correlation [23].

The off-specular scattering originating from holes (see cartoon in Figure 12(b) can also be well identified (see Figure 12 (b')). The off-specular pattern is determined by the Yoneda and super-Yoneda intensity lines. Here the parameters of the perturbation potential are the depth of the holes and the mean diameter of the randomly distributed holes. The depth of holes with $L = 610$ Å coincides with the thickness of the repeat distance of the polymer film (PBMA-PS-PS-PBMA). Assuming a random

distribution of holes their mean diameter was found as $d = 9000$ Å. The size distribution is described by a Lorenzian distribution with exponent -1.5.

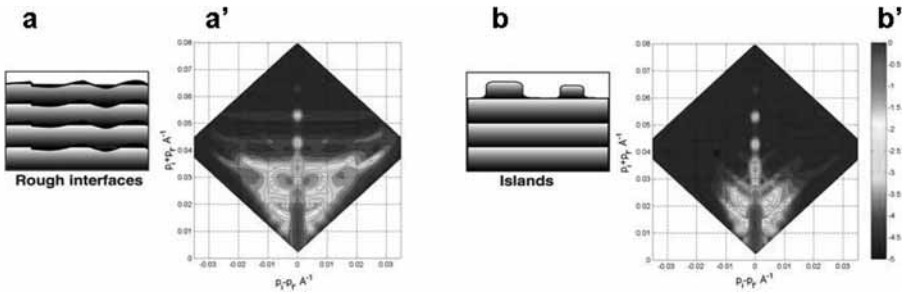

Figure 12. The model and results of calculations for the contributions to Figure 11(b): (a) and (aÕ) off-specular scattering from the interfacial roughness between PS and PBMA; (b) and (bÕ) pattern of off-specular scattering from holes (or islands) on the surface of the ML.

Having identified the features through which the scattering from the interface roughness and surface structure can be characterized, the fit to these regions can be performed along cuts in the 3-d intensity map of Figure 11. The parameters of the perturbation potential used in the DBWA [31,26,23] are an average height $\sigma = 30$ Å centered at the interfaces with an average lateral distance $\xi = 1500$ Å and $\nu = 1.5$ [35]. The overall decay of the higher order Bragg sheets is mainly determined by the conformity parameter and the rms roughness σ. The latter is found as $\sigma = 30$ Å. So, the PBMA-PS interfaces are oscillating back and forward with average amplitude of 30 Å over a surface area with average diameter of 1500 Å and this oscillation is nearly conformally repeated throughout the multilayer stack.

This example demonstrates that the off-specular scattering is roughness-selective, thus different sources of perturbation give rise to different pattern of the scattered intensity.

5.2 Spin-resolved unpolarized neutron off-specular scattering from magnetic multilayers

Unpolarized neutrons scattered from magnetic multilayer self-separate according to the neutron spin state in the dynamical scattering regions of Yoneda scattering and superstructure Bragg-sheet scattering. Strong anomalies in the off-specular scattering originating from magnetic fluctuations in the multilayer are determined by the spin-flip selective process.

In exchange coupled multilayers the interplay between the crystalline anisotropy, interlayer exchange coupling and external magnetic field strength leads to the result that the layer magnetizations in successive Fe-layers in each columnar domain [33] are oriented at a certain *coupling* angle with respect to each other as shown in Figure 13. Here we show that even *unpolarised* neutron off-specular scattering can efficiently be used to determine the configurations of the atomic magnetic moments [37]. Reflectometry experiments have been carried out on the EVA-spectrometer with a wavelength of 5.4 Å and an external magnetic field of 500 G. The sample was a ([Cr(9 Å)/^{57}Fe(68Å)]-x12 /Cr(68Å)) multilayer on a sapphire substrate grown with molecular beam epitaxy. The scattering geometry with specular and off-specular scattering and the sample composition are depicted in Figure 13: here the layer magnetization is decomposed into domains (Figure 13 top view) with an antiferromagnetic interaction perpendicular to the layering (Figure 13 side view). The coupling angle α between the magnetization directions of successive Fe-layers arising due to the external field H is shown in the inset of Figure 13 top view. In Figure 14(a) the 2-dimensional intensity map of specular reflected and off-specular scattered neutrons is shown as a function of p_i and p_f. The specularly reflected intensity along the line $p_i = p_f$ shows the total thickness oscillations as well as the first order Bragg peak ($p_i = p_f = 0.041$ Å^{-1}) corresponding to the bi-layer thickness of 77 Å. The off-specular scattering originates from the domain structure of

the multilayer. It appears as spin-flip Bragg-sheet scattering through the $1/2$ and $3/2$ order Bragg peak positions ($p_i = p_f = 0.0205$ Å^{-1} and $p_i = p_f = 0.0615$ Å^{-1}, respectively) on the reflectivity line as well as along the spin-flip Yoneda scattering parallel to p_i and p_f (Figure 14(a)). A proof of the spin-flip character can be made by spin-analysis of polarized neutrons being scattered from the multilayer [33]. But here it is visible directly through the intensity cut-off due to critical angles. The two critical angles are determined by the two scattering length densities $SLD_n \pm SLD_{mp}$ for the two neutron spin states. SLD_n is the nuclear contribution of the ^{57}Fe and SLD_{mp} is the magnetic contribution from the parallel to the external field component of the magnetic moments M_y^l (Figure 13). So, one critical angle shows up in the units of momentum transfer along $p_i = 0.009$ Å^{-1} and also along $p_f = 0.009$ Å^{-1} due to the use of unpolarized neutrons.

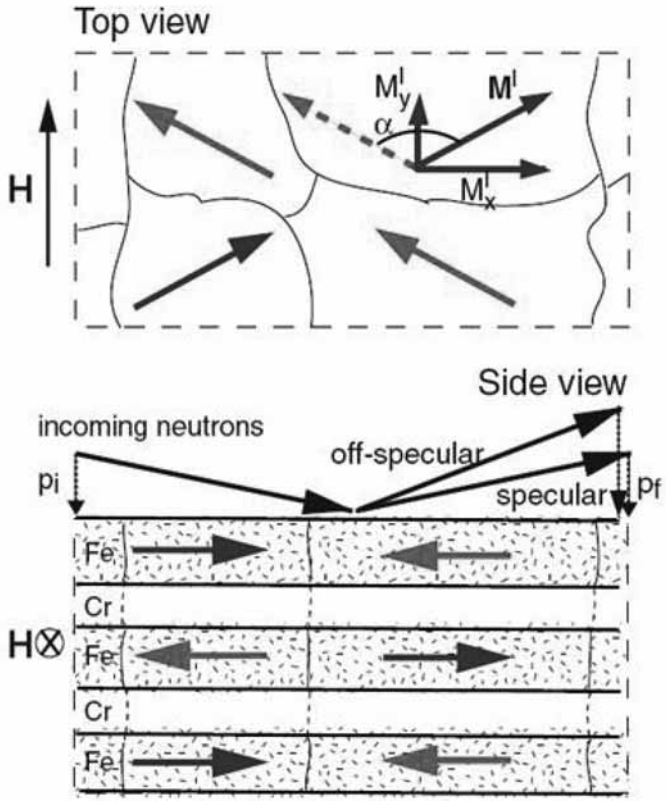

Figure 13. (Top view) sketch of the arrangement of the domain magnetization vectors $\boldsymbol{M}^l$ (thick arrows) in the Fe/Cr ML in the external in-plane magnetic field $\boldsymbol{H}$; schematically, the sample composition is presented; the coupling angle α relates the magnetic moment components of one magnetic layer (within a domain) with the magnetic moment of the adjacent Fe layer(s). (Side view) Scattering geometry and components of magnetic moment perpendicular to the external magnetic field.

It is best visible in the characteristic spikes (marked with C in Figure 14) where the Bragg-sheet scattering runs into the Yoneda scattering and intensity is cut for one spin-state. Any intensity below the mark C originates from the other spin-state. For the sample used in this experiment the other critical angle is imaginary because the difference of $SLD_n - SLD_{mp}$ is negative. Therefore, the off specular scattering extends down to the horizons along $p_i = 0$ and $p_f = 0$ visible in modulated bands parallel to the horizons (*modified Yoneda scattering*) marked with A and B in Figure 14(c) which interfere with the scattering arising due to the total thickness oscillations. The positions of these *Yoneda-bands* depend on

the value of the imaginary critical angle. These effects have been taken into account in the 2-dimensional model fit shown in Figure 14(b). Another critical parameter is given by the substrate potential, which leads to another cut of intensity. For the applied external magnetic field of 500 G this value coincides with the first critical angle marked with C. An extended view of the modeled intensity distribution is shown in Figure 14(c).

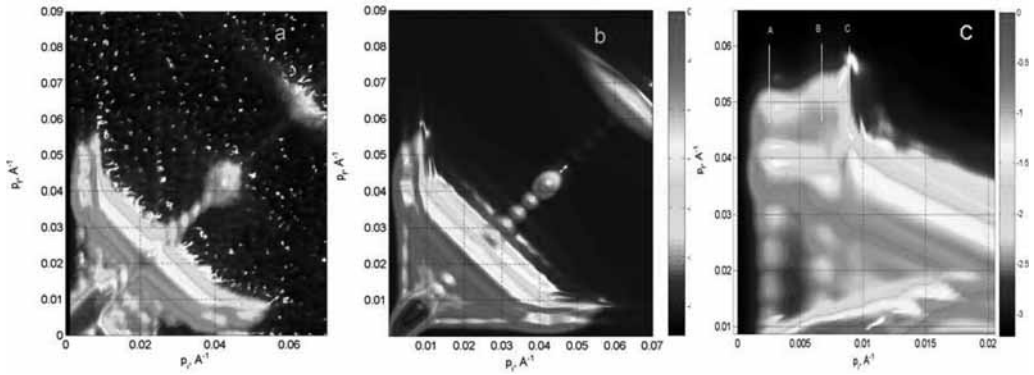

Figure 14. (a) Experimental 2-dimensional intensity map of a Fe/Cr multilayer as a function of $\boldsymbol{p}_i$ and $\boldsymbol{p}_f$, the perpendicular components of the incoming and outgoing wave vector, respectively. The strong intensity along the line $\boldsymbol{p}_i = \boldsymbol{p}_f$ corresponds to the specular reflection. The first order Bragg peak position corresponds to the Fe/Cr bilayer thickness and does not show off-specular scattering. The magnetic spin-flip off-specular Bragg sheet scattering spreads from the $1/2$ and $3/2$ order Bragg peak positions perpendicular to the specular line. (b) Model fit of the 2-dimensional intensity map of a Fe/Cr multilayer shown in Figure 2(a). (c) Extended view on the region of the Bragg-sheet scattering crossing the Yoneda-scattering for experimental data. A and B mark the position of Yoneda scattering related to total thickness oscillations, C is the position of the first critical angle which coincides with the position of the cut-off by the substrate potential.

With the model fit based on the distorted wave Born approximation [32] it is possible to describe all details of the off-specular scattering and to unravel the detailed composition of the layer magnetization in the multilayers system. In particular it has been possible to extract the two scattering length densities related to ^{57}Fe (SLD_n and SLD_{mp}) from the fit to the data obtained with unpolarised neutrons. The knowledge of SLD_{mp} is decisive to determine the coupling angle α of the magnetic moments using for M^l the full atomic magnetic moment of Fe. Consequently, the mean coupling angle can be determined (also as a function of applied field) and related to the GMR effect [34].

In summary, we have demonstrated that rather detailed information on the morphology of materials that are structured on a nanometer scale can be gained using the combination of neutron grazing incidence techniques, comprising reflectometry and off-specular scattering. We show that the details of the internal structure of multilayers are encoded in the two-dimensional map of the intensity scattered by the film. The potential for the synthesis of highly organized structures depends on the aptitude to control not only the distribution of the nano objects but also their morphology and the details of the spatially defined long-range order of the host matrix.

This approach will be applied to a wide range of technologically important systems and can be used to design novel composite architectures.

6 ACKNOWLEDGEMENTS

I want to thank Hans Lauter and Boris Toperverg for our long collaboration and fruitful teamplay, Victor Aksenov and Wienfried Petry for their support during many years. I am indebted to Vladimir Ustinov, Lazar Romashev and Michail Milyaev for our collaboration on magnetic multilayers. I acknowledge the help my colleagues Alexander Petrenko and Alexei Vorobiev for their help during experiments, and

also to Oleg Nikonov for his input in the earlier stage of the work on off-specular scattering. I thank Eric Ressouche for encouragement in writing this manuscript and his patience and help in preparing the French version of the paper. This work was supported by the BMBF (Project 03DU03MU).

References

[1] Ankner, J., Felcher, G., *JMMM* **200** (1999) 741.
[2] Baibich, M.N., Broto, J.M., Fert, A., Nguen Van dau, F., Petroff, F., Etienne, P., Creuzet, G., Friederich, A. and Chazelas, J. *Phys. Rev. Lett* **61**, 2472 (1988).
[3] Binasch, G., Grünberg, P., Saurenbach, F. and Zinn, W., *Phys. Rev. B* **39**, 4828 (1989).
[4] Ambrose, T., Kai Liu, and Chien, C. L., *J. Appl. Phys.* **85**, 6124 (1999).
[5] Strijkers, G.J., Zhou, S.M., Yang, F.Y. and Chien, C.L., *Phys. Rev. B* **62**, 13896 (2000).
[6] Theis-Bröhl, K., Toperverg, B.P., Leiner, V., Westphalen, A., Zabel, H., et al., *Phys. Rev. B* **71**, 020404(R) (2005).
[7] Valden, M., Lai, X., Goodman, D.W., *Science* **281**, 1647 (1998).
[8] Hansen, P.L., et al, *Science* **295**, 2053 (2002).
[9] Semiconductor Quantum Dots, Zunger, A., Ed. *Mater. Res. Soc. Bull* **23** (no2) (1998).
[10] Toperverg, B.P., Felcher, G.P., Metlushko, V.V., Leiner, V., Siebricht, R., Nikonov, O., *Physica B* **283**, 149 (2000).
[11] Kelberg, E.A., Grigoriev, S.V., Okorokov, A.I., et al., *Physica B* **335**, 123 (2003); Grigoriev, S., Grigorieva, N., Vorobiev, A., (http://club.ill.fr/cv/servlet/ReportFind), *ILL Exp Report* 7-09-114 (2004).
[12] Sackmann, E., *Science* **271**, 43 (1996).
[13] Wagner, M. and Tamm, I., *Biophys. J* **79**, 1400 (2000).
[14] Gutberlet, T., Steitz, R., Fragneto, G., Klosgen, B., *J. Phys.: Condens. Matter* **16**, S2469 (2004).
[15] Nelson, D.L. and Cox, M.M., *Lehninger Principles of Biochemistry*, 4th ed. (W.H. Freeman and Company, San Francisco, 2004), Chap.II.
[16] Su, L.Y., Hawkridge, F.M. and Rohten, M.C., *Chem. Biodiversity*, **1**, 1281 (2004).
[17] Beugin, S., Edwards, K., Karlsson M. Ollivon, G., Lesieur, S., *Biophys J* **74**, 3198 (1998).
[18] McGillivray, D.J., Thomas, R.K., Rennie, A.R., Penfold, J., Sivia, D.S., *Langmuir* **19**, 7719 (2003).
[19] Mandel, L. and Wolf, E., *Optical coherence and Quantum optics* (Cambridge Univ. Press, Cambridge 1995).
[20] Schiff, L.I., *Quantum Mechanics*, McGraw_Hill, New York, 1968.
[21] Vineyard, G.H., *Phys. Rev. B* **26**, 4146 (1982).
[22] Mohanty, U. and Rice, S.A., *J. Chem. Phys.* **79**, 2482 (1983).
[23] Sinha, S.K., Sirota, E.B., Garoff, S., Stanley, E., *Phys. Rev. B* **38**, 2297 (1988).
[24] Pynn, R., *Phys. Rev. B* **45**, 602 (1992).
[25] Toperverg, B.P., *Physica B* **297**, 160 (2001).
[26] Toperverg, B.P., Lauter-Pasyuk, V., Lauter, H., Nikonov, O., Ausserre, D., Gallot, Y., *Physica B* **283**, 60 (2000).
[27] Toperverg, B.P., Rühm, A., Donner, W., Dosch, H., *Physica B 267–268*, 198 (1999) ; Rühm, A., Toperverg, B.P., Dosch, H., *Phys. Rev. B* **60**, 16073 (1999).
[28] Parratt, L.G., *Phys. Rev.* **95**, 359 (1954).
[29] Grünberg, P., Schreiber, R., Pang, Y., Brodsky, M., Sowers, H., *Phys. Rev. Lett.* **57**, 2442 (1986); Baibich, M.N., Broto, J.M., Fert, A., Nguen Van Dau, F., Petroff, F., Etienne, P., Creuset, G., Friederich, A., Chazelas, J., *Phys. Rev. Lett.* **61**, 2472 (1988) ; Binach, G., Grünberg, P., Saurenbach, F., Zinn, W., *Phys. Rev. B* **39**, 4828 (1989).

[30] Kiessig, H., *Ann. Phys. Leipzig* **10**, 769 (1931).

[31] te Velthuis, S.G.E., Jiang, J.S., Bader, S.D., Felcher, G.P., *Phys. Rev. Lett*, **89**, 127203 (2002).

[32] Toperverg, B.P., Nikonov, O., Lauter-Pasyuk, V., Lauter, H., *Physica B* **297**, 169 (2001).

[33] Lauter-Pasyuk, V.V., Lauter, H.J., Toperverg, B.P., Romashev, L., Ustinov, V., *Phys. Rev. Lett.* **89**, 167203 (2002).

[34] Lauter-Pasyuk, V.V., Lauter, H.J., Toperverg, B.P., Nikonov, O., Kravtsov, E., Romashev, L., Ustinov, V., *J. Magn. Magn. Mater.* **226–230**, 1694 (2001).

[35] Lauter-Pasyuk, V.V., Lauter, H.J., Toperverg, B.P., Petrenko, A., Schubert, D., Schreiber, J., Burcin, M., Aksenov, V., *Appl. Phys. A* **74** [Suppl.], S528 (2002).

[36] Ming, Z.H., Krol, A., Soo, Y.L., Kao, Y.H., Park, J.S., Wang, K.L., *Phys. Rev. B* **47**, 16373 (1993).

[37] Lauter, H.J., Lauter-Pasyuk, V.V., Toperverg, B.P., Romashev, L., Ustinov, V., Kravtsov, E., Vorobiev, A., Nikonov, O., *J. Major, Appl. Phys. A* **74** [Suppl.], S1557 (2002).